



In-situ enriching active sites on co-doped Fe-Co₄N@N-C nanosheet array as air cathode for flexible rechargeable Zn-air batteries

Qiucheng Xu, Hao Jiang*, Yuhang Li, Da Liang, Yanjie Hu, Chunzhong Li*

Key Laboratory for Ultrafine Materials of Ministry of Education, Shanghai Engineering Research Center of Hierarchical Nanomaterials, School of Materials Science and Engineering, East China University of Science and Technology, Shanghai 200237, China



ARTICLE INFO

Keywords:
Bifunctional electrocatalysts
Flexible electrode
MOF derivative
Co₄N
Zn-air battery

ABSTRACT

The sluggish oxygen evolution reaction (OER) and oxygen reduction reaction (ORR) kinetics in air cathode severely restrain the development of the reversible Zn-air battery. Herein, we report the design and synthesis of co-doped Fe-Co₄N@N-C nanosheet array derived from MOF precursor on carbon cloth as the dual-functional electrocatalyst to boost the reaction kinetics. The Fe, N co-doping significantly promotes the generation of abundant Pyridinic-N-M active sites for ORR due to the strong coordination effect between metal center and pyridinic nitrogen. The enriched Co³⁺ sites concurrently motivate the formation of targeted *OOH intermediates during OER with decreased charge transfer resistance. Such electrocatalyst therefore delivers high catalytic activity for both ORR and OER. When applied as air cathode for liquid Zn-air battery, the device exhibits a high specific energy density of 934 Wh kg⁻¹ with excellent cycling stability, which is superior to the referenced Pt and Ru-based Zn-air batteries. Flexible solid-state Zn-air battery can also achieve a high volumetric power density of 72 mW cm⁻³ and good cycling durability under different bending states. This work gives a facile and cost-efficient strategy to construct bifunctional flexible electrode with enriched active sites for Zn-air batteries.

1. Introduction

Rechargeable Zn-air batteries with high theoretical specific energy density (1084 Wh kg⁻¹) and good security are considered as promising energy storage device for developing next-generation portable electronics [1–3]. One crucial challenge for reversible Zn-air batteries is that their energy conversion efficiency is still limited by the sluggish oxygen evolution reaction (OER) and oxygen reduction reaction (ORR) kinetics in air cathode with high overpotential [4–6]. Noble metal based Ru/C and Pt/C catalysts can effectively decrease their respective reaction overpotential, whereas their high cost and bad stability greatly block large-scale application [7–9]. Low-cost transition metal nitrides possess abundant M–N covalent bonds and M–M metal bonds, which can not only promote the formation of key OER intermediates but also enhance the adsorption of oxygen free radical (O₂[·]). These advantages have recently attracted considerable attention for developing them as dual-functional oxygen reaction (OER&ORR) electrocatalysts [10–12]. However, the poor electron donating ability of metal center inside metal nitrides slows the conversion kinetics of the adsorbed O₂[·] to hydroxyl species resulting in the unsatisfied ORR performance [13,14].

The modulation of coordination structure and atomic configuration of catalyst is an effective way to improve electron donating ability of

active site for enhancing the ORR kinetics [15–18]. Recent experimental and theoretic studies have proved the strong coordination between metal center and Pyridinic-N could promote the formation of Pyridinic-N-M active sites, where the electron enriched Pyridinic-N effectively accelerate the charge transfer to metal center so as to greatly improve ORR activity [19,20]. For example, a novel hybrid catalyst composed of the Co₄N nanoparticles embedded in N-doped carbon (N-C) fibers has been prepared by the pyrolysis of ZIF-67/polypyrrole nanofibers network [21]. The strong interaction between Co₄N and N-C induces the formation of abundant Co-N-C active sites, exhibiting a high half-wave potential of 0.8 V. Notably, there are various coordination types of N-C such as Pyridinic-N, Pyrrolic-N, Graphitic-N and so on. The Pyridinic-N coordination for forming the ideal Pyridinic-N-M active sites could be hard to controllably generate [22–24]. On the other hand, the self-supported flexible electrodes can avoid the use of polymer binders and expedite electron transfer for achieving flexible Zn-air batteries with high capacity and stability [25,26]. However, it is still a great challenge to develop Pyridinic-N-M active sites enriched metal nitride/N-doped carbon composite as self-supported flexible electrode for reversible Zn-air batteries.

Imidazole metal organic framework (MOF) have high nitrogen content and uniform metal coordination structure, which is suitable to

* Corresponding authors.

E-mail addresses: jianghao@ecust.edu.cn (H. Jiang), czli@ecust.edu.cn (C. Li).

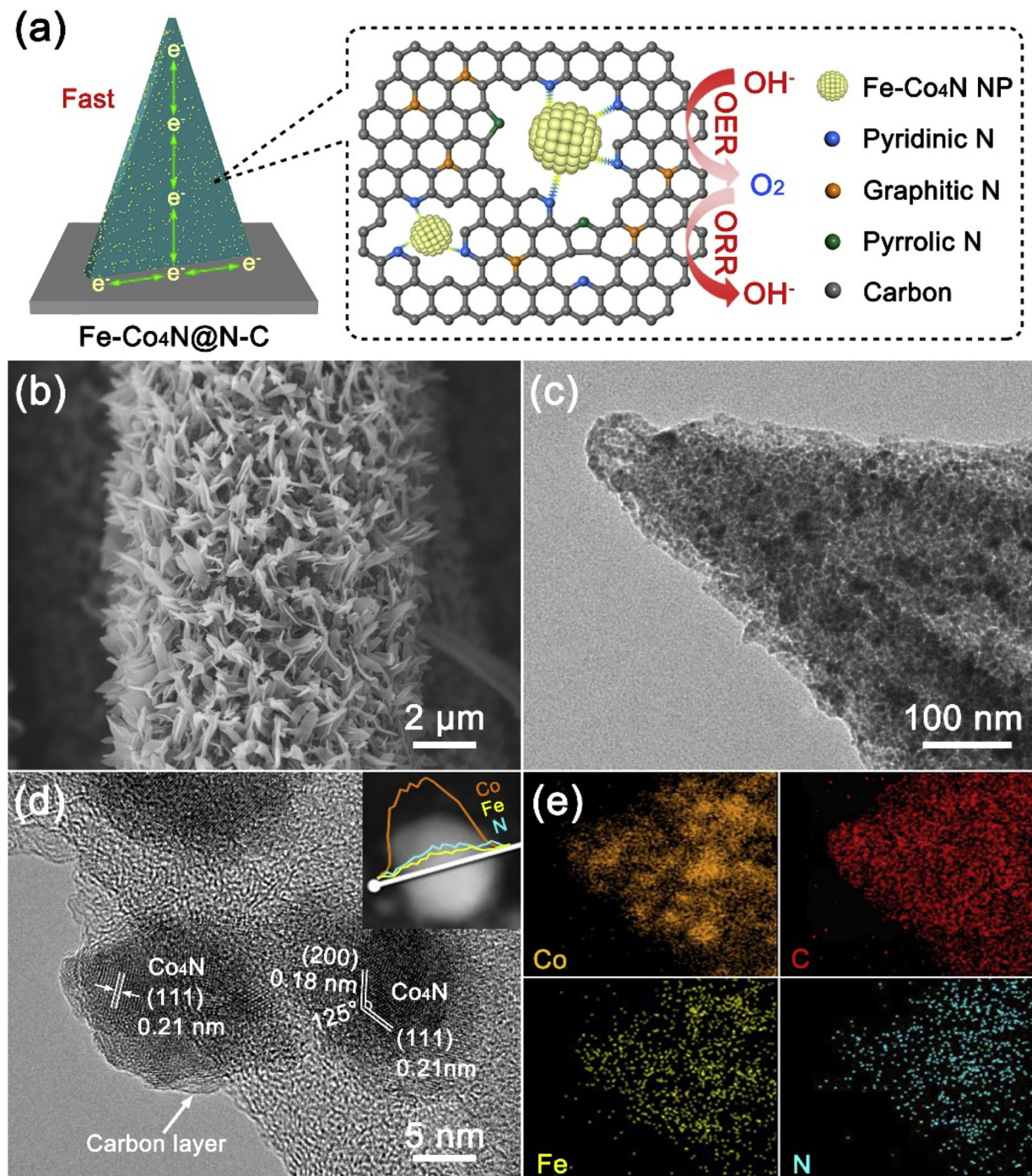


Fig. 1. a) Schematic illustration of the Fe-Co₄N@N-C nanosheet grown on carbon cloth for dual-functional oxygen reaction. b) SEM, c) high-magnification TEM, d) high-resolution TEM images and e) TEM-EDS mapping of the Fe-Co₄N@N-C electrocatalyst. The inset in (d) exhibits the EDS line scanning profile recorded from a single Fe-Co₄N nanoparticle.

develop oxygen reaction electrocatalysts with abundant M–N–C active sites. Inspired by this, we herein successfully construct the co-doped Fe-Co₄N@N-C nanosheet array derived from the zeolitic imidazolate framework precursor on flexible carbon cloth by a facile combined carbonization-ammonization process. As shown in Fig. 1a, such hybrid catalyst with strong coordination effect between the Fe-Co₄N and N–C possesses a large number of Pyridinic-N–M species as active sites for improving ORR catalysis. The enriched Co³⁺ sites can also motivate the formation of targeted *OOH intermediates during OER with fast charge transfer. Consequently, the Fe-Co₄N@N-C electrocatalyst exhibits superior catalytic activity toward the OER ($\eta_{10} = 318$ mV) and ORR ($E_{1/2}$

$= 0.83$ V) in 0.1 M KOH electrolyte. When applied as air cathode for liquid Zn-air battery, a high specific energy density of 934 Wh kg⁻¹ and excellent cycle durability can be obtained, which is superior to the referenced Pt and Ru-based Zn-air batteries. Furthermore, the self-supported Fe-Co₄N@N-C electrocatalyst can also assemble as the flexible solid-state Zn-air battery. The device presents a high volumetric power density of 72 mW cm⁻³ and good cycling durability under different bending states. This work provides a facile and cost-efficient strategy to construct bifunctional flexible electrode with enriched active sites for reversible Zn-air batteries.

2. Experimental

2.1. Catalysts synthesis

The carbon cloth ($2 \times 5 \text{ cm}^2$) was firstly pretreated in a mixed acid solution containing $\text{HNO}_3/\text{H}_2\text{SO}_4$ (volume ratio of 1:3) for 24 h. Then, the 2D Co-MOF was grown on its surface via a facile solution reaction. Typically, 0.4 M of 2-methylimidazole aqueous solution (50 mL) and 0.05 M of $\text{Co}(\text{NO}_3)_2 \cdot 6\text{H}_2\text{O}$ aqueous solution (50 mL) were simultaneously poured into a clean container with strong stirring. Afterward, the carbon cloth was quickly inserted into the above mixture solution and stood for 2 h. The 2D Co-MOF was obtained by cleaning in the water and drying at 60°C overnight. Further, the 2D Co-MOF on the carbon cloth was immersed into a $\text{K}_3[\text{Fe}(\text{CN})_6]$ aqueous solution (0.05 M) under room temperature and stayed for 10 min to prepare the 2D Co/Fe-MOF precursor. Finally, the $\text{Fe-Co}_4\text{N}@\text{N-C}$ were achieved by annealing the precursor in a flowing H_2/Ar (1:19) gas at 700°C for 2 h with a heating rate of 1°C min^{-1} and then in pure NH_3 gas at 350°C for 2 h with a heating rate of 5°C min^{-1} . For preparing the $\text{Co}_4\text{N}@\text{N-C}$ catalyst, all the procedures are same as those of the $\text{Fe-Co}_4\text{N}@\text{N-C}$ catalyst except the immersion procedure in the $\text{K}_3[\text{Fe}(\text{CN})_6]$ aqueous solution. For preparing the $\text{Co}@\text{N-C}$ and the $\text{CoFe}@\text{N-C}$ catalysts, only carbonization process was performed for the 2D Co-MOF and 2D Co/Fe-MOF precursors. The typical mass loading of the $\text{Fe-Co}_4\text{N}@\text{N-C}$ electrocatalyst on carbon cloth is about 1 mg cm^{-2} .

2.2. Structural characterization

The crystal structure of the electrocatalysts was characterized by X-ray diffraction (XRD) with a scan rate of 3° min^{-1} (Rigaku D/Max 2550, Cu K_α radiation). The morphology of the electrocatalysts was observed by field emission scanning electron microscopy (FESEM, Hitachi, S-4800, 10 kV) and field emission transmission electron microscopy (FETEM, JEOL, JEM-2100 F) with an X-ray energy dispersive spectrometer (EDS). The X-ray photoelectron spectroscopy (XPS) was used to analyze the surface chemical state of the electrocatalysts by a Thermo Scientific ESCALAB 250Xi. Raman measurement was performed by using a spectrometer (Via + Reflex) at an excitation wavelength of 514 nm. The O_2 temperature-programmed desorption (O_2 -TPD) spectra were measured by an Auto Chem-II2920 (Micromeritics) with a thermal conductivity detector. Typically, the sample was pretreated at 250°C for 1 h in He flow and then cool down to 20°C . The O_2 adsorption was carried out by exposing the sample to a flow of 5% O_2/He at 20°C for 1 h. After flushing in He flow for 20 min, the O_2 -TPD was recorded from 50 to 600°C with a heating rate of $10^\circ\text{C min}^{-1}$.

2.3. Electrochemical measurements

All the electrochemical measurements were tested in 0.1 M KOH electrolyte ($\text{pH} = 13$) by a three electrode system consisting of as-prepared working electrodes, the graphite counter electrode and Ag/AgCl (saturated KCl) reference electrode. All potentials were calibrated to a reversible hydrogen electrode (RHE) by the equation as follow: $E \text{ (vs. RHE)} = E \text{ (vs. Ag/AgCl)} + 0.1976 + 0.0591 \times \text{pH}$. For ORR test, the powder samples were firstly prepared as ink solution (10 mg of the powder, 60 μL of 5 wt% Nafion solution, 0.44 mL of ethanol and 0.5 mL of distilled water mixed under ultrasonic condition) and then dropped onto the rotating disk electrode (the loading $\sim 0.5 \text{ mg cm}^{-2}$). The linear sweep voltammetry (LSV) curves of samples was measured at a scanning rate of 5 mV s^{-1} with different rotating speeds (400, 625, 900, 1225 and 1600 rpm). The electron transfer number (n) of ORR was calculated through Koutecky-Levich equation: $1/J = 1/J_L + 1/J_K = 1/(B\omega^{1/2}) + 1/J_K$ and $B = 0.62nFC_0D_0^{2/3}V^{1/6}$, where J , J_K and J_L are the measured, kinetic and limiting current densities, respectively, ω is the rotating speed (rad s^{-1}), C_0 is the bulk concentration of O_2 ($1.2 \times 10^{-6} \text{ mol cm}^{-3}$), F is the Faraday constant (96485 C mol $^{-1}$), D_0 is the diffusion

coefficient of O_2 in 0.1 M KOH ($1.9 \times 10^{-5} \text{ cm}^2 \text{ s}^{-1}$) and V is the kinematic viscosity of the electrolyte ($0.01 \text{ cm}^2 \text{ s}^{-1}$). The hydrogen peroxide yields was caculated using the equation as follow: $\% \text{ H}_2\text{O}_2 = 100(2I_R/N)/(I_D + I_R/N)$, where I_R , I_D and N were the ring current, disk current and the ring collection efficiency of the Pt ring disk (0.37), respectively. For OER test, the linear sweep voltammetry (LSV) curves were measured at a scanning rate of 1 mV s^{-1} and the data were 95% iR -corrected according to the solution resistance (Ω). Electrochemical impedance spectroscopy (EIS) measurements were performed by an Autolab PGSTAT302 N at an OER overpotential of 300 mV with a test frequency ranging from 0.01 Hz to 100 KHz. The cycle-voltage measurements were used to measure double-layer capacitance (C_{dl}) by changing scan rates from 40 to 120 mV s^{-1} . The ECSA of samples can be calculated from the equation: $\text{ECSA} = C_{dl}/C_s$, where C_s represents specific capacitance ($25 \mu\text{F cm}^{-2}$ for Co-based materials as the standard value in alkaline media).

2.4. Assembly of rechargeable Zn-air batteries

The aqueous Zn-air batteries were tested by a two electrode system in 6.0 M KOH aqueous electrolyte with 0.2 M zinc acetate. The as-prepared electrodes were attached to carbon paper (HESEN HCP130) to form the air electrode. Zn foil (0.3 mm thickness) was served as anode. The active area of air electrode and Zn foil was 0.785 cm^2 . Cycle test was characterized by galvanostatic charge/discharge at 5 mA cm^{-2} for 10 min each pulse. The flexible solid-state Zn-air batteries were assembled into a sandwich structure, where the as-prepared catalyst and Zn foil were used as self-supported air electrode and anode, respectively. The polyacrylamide (PAM) gel polymer was prepared as solid electrolyte. Typically, 2 g of acrylamide was added into 20 mL deionized water stirring at room temperature under nitrogen protection for 30 min. Then, 10 mg ammonium sulfate and 2 mg N,N'-methylene-bisacrylamide were dissolved in the above solution serving as initiator and crosslinking agent, respectively. After reacting for 15 min, the solution was transferred into the glass mold keeping at 50°C in a vacuum for 4 h to obtain the PAM gel electrolyte. Before testing, the PAM gel electrolyte require to soak in the solution containing 6.0 M KOH and 0.2 M zinc acetate for 30 min.

3. Results and discussion

3.1. Synthesis and characterizations of $\text{Fe-Co}_4\text{N}@\text{N-C}$ electrocatalyst

The fabrication procedure of the $\text{Fe-Co}_4\text{N}@\text{N-C}$ nanosheets array electrocatalyst is schematically demonstrated in Fig. S1. First, the nanosheet-like cobalt metal organic framework (2D Co-MOF) is grown on the acidified carbon cloth by a facile solution reaction of $\text{Co}(\text{NO}_3)_2$ and 2-methylimidazole (2-MIM). Then, the as-obtained 2D Co-MOF on carbon cloth is immersed into a $\text{K}_3[\text{Fe}(\text{CN})_6]$ aqueous solution under room temperature and stay for a certain time. In this step, the 2D Co/Fe-MOF is formed by the ligands exchange between $[\text{Fe}(\text{CN})_6]^{3-}$ and 2-MIN [27]. The morphology of 2D Co-MOF and 2D Co/Fe-MOF is shown in Fig. S2. After the carbonization at 700°C under H_2/Ar gas and the subsequent ammonization at 350°C under NH_3 gas, the $\text{Fe-Co}_4\text{N}@\text{N-C}$ nanosheet array is obtained on the carbon cloth (for more details see Experimental section). Fig. 1b and Fig. S3 exhibit the scanning electron microscopy (SEM) images of the as-expected nanosheets array architecture. These nanosheets with thickness of $\sim 45 \text{ nm}$ are orderly grown on the carbon cloth. The thickness of $\text{Fe-Co}_4\text{N}@\text{N-C}$ nanosheet was also measured by AFM (Fig. S4). The high-magnification transmission electron microscopy (TEM) image (Fig. 1c) presents the top-end of single nanosheet, where nanoparticles with size of $\sim 20 \text{ nm}$ are uniformly incorporated in the carbon framework. The graphitization of carbon layer is low, as shown in the high-resolution TEM image (Fig. 1d). Moreover, the lattice fringe spacing of 0.18 nm and 0.21 nm with a dihedral angle of 125° can be assigned to the (200) and (111)

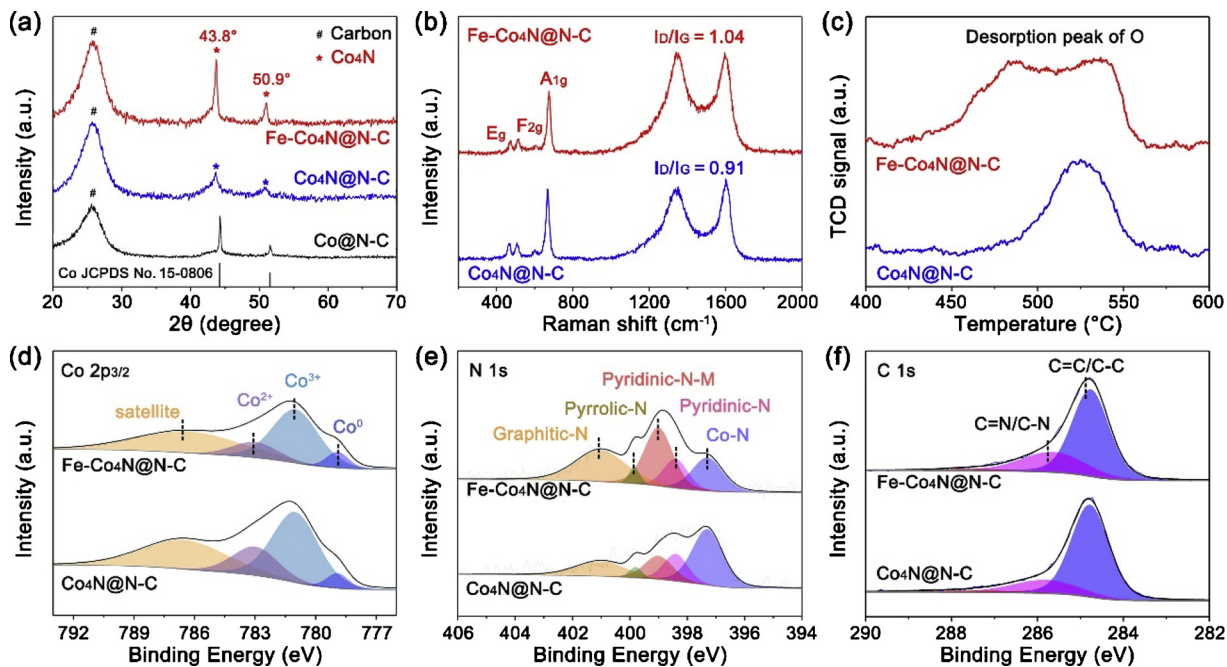


Fig. 2. a) XRD patterns of the Fe-Co₄N@N-C, the Co₄N@N-C and the Co@N-C electrocatalysts. b) Raman spectra, c) O₂-TPD spectra and d-f) high-resolution XPS spectra for Co 2p_{3/2}, N 1s and C 1s of the Co₄N@N-C and the Fe-Co₄N@N-C electrocatalysts.

planes of Co₄N [28], respectively, indicating that well crystallized Co₄N nanoparticles are embedded in the carbon nanosheet. The corresponding selected area electron diffraction (SAED) pattern (Fig. S5) also verifies the formation of crystallized Co₄N. The inset exhibits the EDS line scanning profile recorded from a single nanoparticle displaying a gradient distribution of the Co, Fe and N elements. This phenomenon proves that the Fe element are successfully doped in the Co₄N nanoparticle. Furthermore, the high-angle annular dark field (HAADF) image and corresponding EDS mapping are shown in Fig. S6 and Fig. 1e. The bright region belongs to Fe-Co₄N nanoparticles showing greater distribution of Co, Fe, and N elements. Such result further certifies that the Fe-doped Co₄N nanoparticles are embedded in the N-doped carbon nanosheets. The Fe-doped molar ratio is ~ 5% calculated by the inductively coupled plasma mass spectroscopy (ICP-MS) and TEM-EDS results (Fig. S7).

The X-ray diffraction (XRD) patterns of the Fe-Co₄N@N-C, the Co₄N@N-C and the Co@N-C electrocatalysts are given in Fig. 2a. The Fe-Co₄N@N-C and Co₄N@N-C possess two diffraction peaks at 43.8° and 50.9° corresponding to the (111) and (200) crystal planes of Co₄N, which well match the reported references [21,28]. For the Co@N-C, its characteristic peaks show a right shift of 0.6° by compared with the Co₄N@N-C, which is assigned to Co (JCPDS No.15-0806). Such shift suggests the Co metal completely convert into Co₄N during ammonization process. All samples exhibit a diffraction peak at 26.4° assigned to the (002) plane of carbon (JCPDS No.26-1076). The XRD pattern of the CoFe@N-C is also shown in Fig. S8. It has additional peak at 45.1° attributed to the Co₂Fe₃ alloy (JCPDS No.48-1818) by compared with the Co@N-C, illuminating the Fe doped into Co metal lattice. Fig. 2b provides Raman spectra of the Fe-Co₄N@N-C and the Co₄N@N-C electrocatalysts. Two identical peaks located at 1350 cm⁻¹ and 1590 cm⁻¹ are related to the D and G bands of graphite, respectively [29]. The intensity ratio of D and G bands (I_D/I_G) can reflect the graphitization degree of carbon [30]. The Fe-Co₄N@N-C electrocatalyst has a higher I_D/I_G of 1.04 than the Co₄N@N-C electrocatalyst of 0.91, indicating its relatively low graphitization degree. This result also implies that the introduced [Fe(CN)₆]³⁻ ligand can motivate the in-situ formation of defective carbon (N doped carbon) during carbonization. Moreover, the Fe-Co₄N@N-C and the Co₄N@N-C electrocatalysts both

show the E_g (474 cm⁻¹), F_{2g} (515 and 608 cm⁻¹) and A_{1g} (675 cm⁻¹) vibration modes of Co elements, which further suggests the formation of the Co₄N [31]. The oxygen temperature-programmed desorption (O₂-TPD) spectra of the Fe-Co₄N@N-C and the Co₄N@N-C electrocatalysts are further performed to understand the potential oxygen adsorption sites on the catalysts, as shown in Fig. 2c. It can be found that the Fe-Co₄N@N-C exhibits two oxygen desorption peaks while the Co₄N@N-C only have one desorption peak. This result implies the Fe-Co₄N@N-C possesses an extra oxygen adsorption active site in contrast with the Co₄N@N-C for improving the ORR activity.

To investigate the chemical bonding state, the high-resolution X-ray photoelectron spectroscopy (XPS) spectra of the Fe-Co₄N@N-C and the Co₄N@N-C electrocatalysts are analysed. Fig. 2d provides the deconvolution of Co 2p_{3/2} XPS spectra, where three peaks at 778.9, 781.1 and 783.1 eV are attributed to Co⁰, Co³⁺ and Co²⁺, respectively [32–34]. The metallic state Co species (Co⁰) is derived from the Co-Co bonds inside the unit cell of Co₄N. The oxidized states of Co species (Co³⁺ and Co²⁺) suggest electron transfer from Co to N atoms. It can be found the Fe-Co₄N@N-C exhibits a larger Co³⁺ peak area ratio of 71.3% by comparing with the Co₄N@N-C of 65.3% (calculated by the area value of Co³⁺/(Co⁰ + Co²⁺ + Co³⁺)). The Co³⁺ sites are crucial to fast the formation of key OER intermediates (*OOH), which implies the improved OER activity of the Fe-Co₄N@N-C [35,36]. The XPS spectra of Fe 2p_{3/2} for the Fe-Co₄N@N-C electrocatalyst are shown in Fig. S9. The Fe element presents oxidized states (Fe³⁺ and Fe²⁺), which indicates the Fe dopant occupy the Co sites and bond with N atoms [37]. The bonding configuration of N atoms can be further explored by high-resolution XPS N 1s spectra (Fig. 2e and Fig. S10). The peak at 397.3 eV represents the characteristic peak of Co-N bond in Co₄N, which not exists in the Co@N-C and the CoFe@N-C electrocatalysts [31]. Additional four peaks arising from 398.4, 399, 399.8 and 401 eV corresponded to Pyridinic-N, Pyridinic-N-M, Pyrrolic-N and Graphitic-N species, respectively [23]. The Pyridinic-N-M species, which stems from the strong coordination between the Pyridinic-N and metal center (e.g. Fe and Co), is wildly reported as highly active sites for ORR [38–41]. The content of various N-C bonds relative to total elements for different samples are summarized in Table S1. The Fe-Co₄N@N-C electrocatalyst shows an increased Pyridinic-N-M content (2.84%) and a

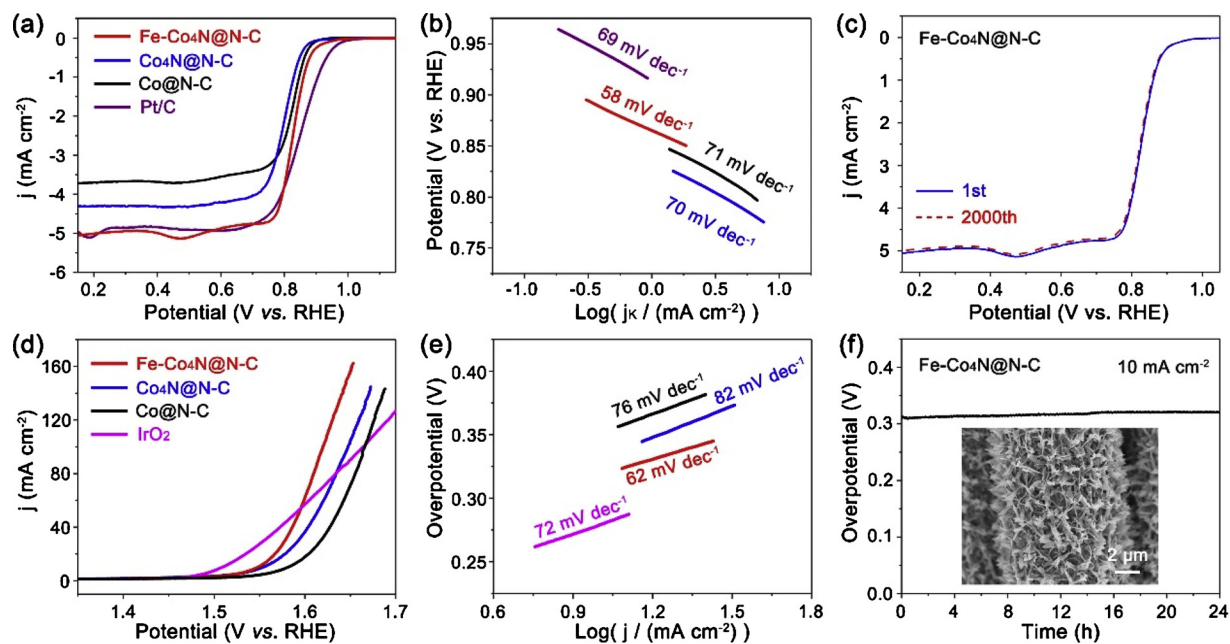


Fig. 3. a) ORR polarization curves tested at 1600 rpm of the Fe-Co₄N@N-C, the Co₄N@N-C, the Co@N-C and Pt/C electrocatalysts, b) the corresponding Tafel plots, c) polarization curves of the Fe-Co₄N@N-C electrocatalysts before and after 2000 potential sweeps for ORR test; d) OER polarization curves of the Fe-Co₄N@N-C, the Co₄N@N-C, the Co@N-C and IrO₂ electrocatalysts, e) the corresponding Tafel plots and f) stability tests of the Fe-Co₄N@N-C by chronopotentiometry measurements at 10 mA cm⁻². The inset in (f) exhibits the SEM image of Fe-Co₄N@N-C electrocatalyst after OER stability tests.

decreased Co-N content (1.76%) compared with the Co₄N@N-C electrocatalyst (1.04% and 2.66%), which suggests that the Fe dopant partly replace the Co species in Co-N bond and improve the in-situ formation of abundant ORR active sites (especially Pyridinic-N-M) during synthesis process. Moreover, the Fe-Co₄N@N-C electrocatalyst exhibits a high Graphitic-N content of 2.70% implying an enhanced electrical conductivity. The XPS C 1s spectra are further provided in Fig. 2f, where the Fe-Co₄N@N-C contains more C = N/C-N species than the Co₄N@N-C in agreement with the XPS N 1s spectra results. According to the above discussion, it can be concluded that abundant active sites with well modified Co and N configuration are in-situ generated inside Fe-Co₄N@N-C, which implies its excellent electrochemical performance.

3.2. Electrochemical activity of Fe-Co₄N@N-C electrocatalyst

The ORR and OER activity of the Fe-Co₄N@N-C, the Co₄N@N-C and the Co@N-C electrocatalysts are tested by three-electrode system in 0.1 M KOH electrolyte. Fig. 3a shows the polarization curves recorded by rotating disk electrode at 1600 rpm. The half-wave potential ($E_{1/2}$) and limiting current density of the Fe-Co₄N@N-C are 0.83 V and 5 mA cm⁻², superior than those of the Co₄N@N-C and the Co@N-C. The Fe-Co₄N@N-C also exhibits the lowest Tafel slope of 58 mV dec⁻¹, as shown in Fig. 3b, which indicates its fast ORR kinetics. The ORR kinetics are further evaluated by performing LSV measurement at the rotating speeds from 400 to 1600 rpm and constructing the corresponding Koutecky-Levich (K-L) plots (Fig. S11). By calculating the slope of the K-L plots, the electron transfer number (n) of ORR can be obtained. The calculated n for the Fe-Co₄N@N-C (3.89) is higher than the Co₄N@N-C (3.55) and the Co@N-C (3.23), which suggests the Fe-Co₄N@N-C electrocatalyst tends to react through an ideal four-electron ORR pathway [42,43]. The RRDE approach was further measured to determine the hydrogen peroxide yield. The ring current (I_R) and the calculated hydrogen peroxide yield (%) of Fe-Co₄N@N-C and Pt/C are shown in Fig. S12. The Fe-Co₄N@N-C shows a low H₂O₂ yield below 5% at 0.6–0.8 V, indicating its four-electron-dominated ORR pathway. The stability test is measured by performing the polarization curves

before and after 2000 CV cycles in O₂-saturated 0.1 M KOH (Fig. 3c). The Fe-Co₄N@N-C electrocatalyst shows a negligible variation of the LSV curves, indicating its excellent ORR stability. On the other hand, the OER polarization curves are shown in Fig. 3d, where the Fe-Co₄N@N-C electrocatalyst can each 100 mA cm⁻² at a small overpotential of 390 mV lower than those of the Co₄N@N-C (418 mV), Co@N-C (436 mV) and the commercial IrO₂ (434 mV). To explore the oxygen generation kinetics of these samples, their Tafel slopes are exhibited in Fig. 3e. The Fe-Co₄N@N-C electrocatalyst presents the smallest Tafel slopes of 62 mV dec⁻¹, implying its rapid OER kinetics. This feature can also be evidenced by the electrochemical impedance spectroscopy (EIS) measurement, as shown in Fig. S13 and Table S2. The high-frequency and low-frequency response in Nyquist plots are assigned to the solution resistance (R_s) and charge-transfer resistance (R_{ct}) during OER catalysis, respectively. The Fe-Co₄N@N-C possesses a R_{ct} of ~13.6 Ω much lower than those of the Co₄N@N-C (~19.3 Ω) and the Co@N-C (~41.4 Ω), suggesting its exceptional reaction kinetics [44]. Moreover, the electrochemically active surface area (ECSA) of electrocatalysts is calculated from their double-layer capacitance results (Fig. S14). The Fe-Co₄N@N-C electrocatalyst has a higher ECSA (80 cm²) than those of the Co₄N@N-C (54 cm²) and Co@N-C (27 cm²). This results indicate that the Fe, N co-doping can increase the formation of Co³⁺ electroactive sites for adsorbing the OH- and therefore promote the conversion of key intermediates (*OOH) during OER. The high resolution XPS O 1s spectra after OER are provided to prove this enhancement, as shown in Fig. S15, where the Fe-Co₄N@N-C exhibits a higher *OOH content of 22.1% by compared with the Co₄N@N-C of 13.2%. The durability of the Fe-Co₄N@N-C was tested by chronopotentiometry measurements (Fig. 3f). It shows an outstanding stability with negligible potential degradation and almost no morphology changes at 10 mA cm⁻² for over 24 h. Based on the aforementioned discussion, the remarkable ORR and OER performance of the Fe-Co₄N@N-C electrocatalyst can be mainly ascribed to the in-situ enriched active sites with greatly improved reaction kinetics. The Fe,N co-doping not only motivate the formation of ideal Pyridinic-N-Co/Fe species as active sites for ORR, but also regulate Co configuration with more Co³⁺ sites for promoting the generation of targeted *OOH intermediates during OER.

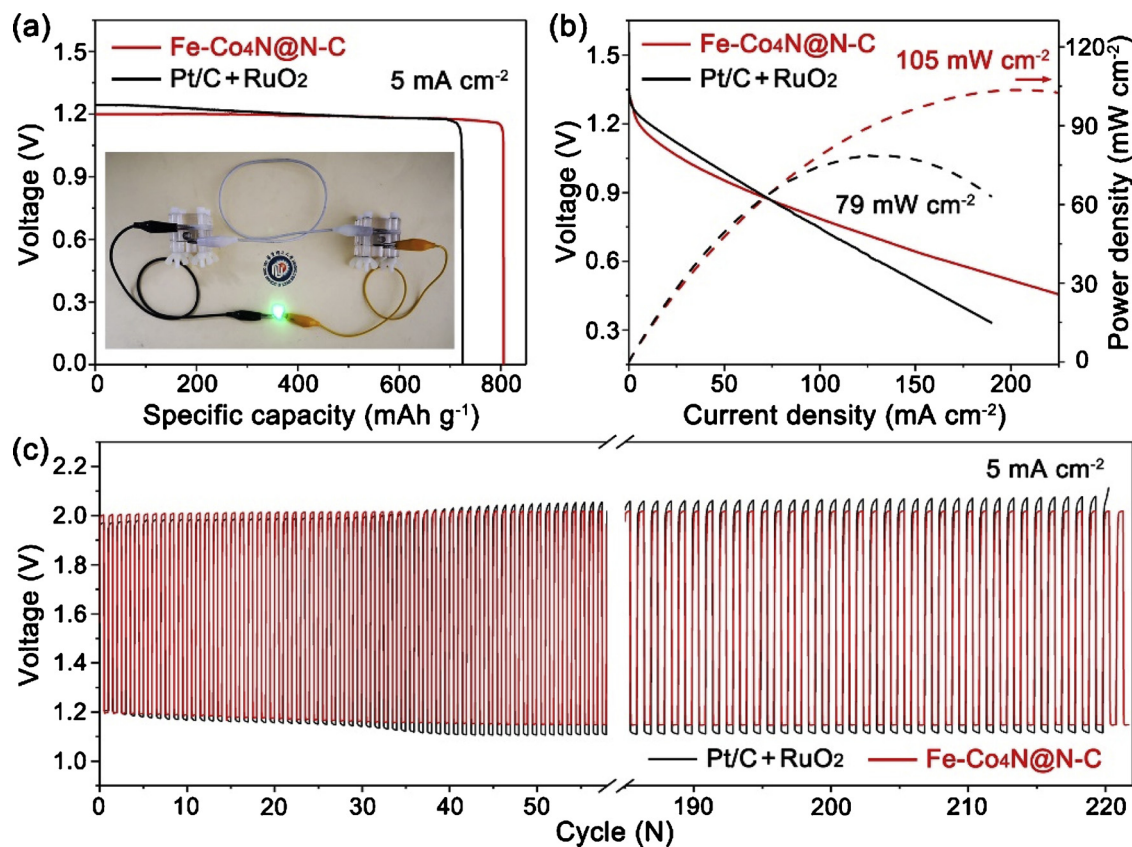


Fig. 4. a) Specific discharging capacities curves, b) discharge polarization curves and the corresponding power density, c) charge and discharge cycling curves at 5 mA cm⁻² of the Fe-Co₄N@N-C and Pt/C + RuO₂ electrocatalysts assembled rechargeable liquid Zn-air batteries. The inset in panel (a) shows the photograph of a green light-emitting diode (LED, 2.2 V) powered by two liquid Zn-air batteries in series, which use the self-supported Fe-Co₄N@N-C electrocatalyst as air-electrode.

3.3. Rechargeable Zn-air battery studies of Fe-Co₄N@N-C electrocatalyst

To evaluate the practical applicability of the electrocatalysts, the rechargeable liquid Zn-air batteries were assembled. The self-supported Fe-Co₄N@N-C electrocatalyst is attached to the carbon paper with gas diffusion layer (GDL) before served as the air electrode. For the referenced 20% Pt/C + RuO₂ sample, the mixed powder (mass ratio 1:1) is deposited on the carbon cloth with similar mass loading to that of the Fe-Co₄N@N-C before using as air cathode. The polished zinc foil and 6.0 M KOM aqueous solution with 0.2 M Zn(CH₃COO)₂ are used as anode and electrolyte, respectively. The open-circuit voltage of all samples is shown in Fig. S16. The Fe-Co₄N@N-C electrocatalyst presents the highest open-circuit voltage of 1.46 V. Fig. 4a and Fig. S17 demonstrate the specific discharging capacities (normalized to the zinc consumed mass) curves. A high specific capacity of 806 mA h g⁻¹ can be obtained for the Fe-Co₄N@N-C at 5 mA cm⁻², which is much higher than Pt/C + RuO₂ of 725 mA h g⁻¹, Co₄N@N-C of 661 mA h g⁻¹ and Co@N-C of 621 mA h g⁻¹. Their corresponding energy density also calculated as the Fe-Co₄N@N-C (934 Wh kg⁻¹), Pt/C + RuO₂ (906 Wh kg⁻¹), Co₄N@N-C (758 Wh kg⁻¹) and Co@N-C (694 Wh kg⁻¹). The inset exhibits the photograph of a green light-emitting diode (LED, 2.2 V) powered by two liquid Zn-air batteries (Fe-Co₄N@N-C) in series. The discharge polarization curves and corresponding power density curves are shown in Fig. 4b and Fig. S18. The Fe-Co₄N@N-C electrocatalyst presents better discharging performance (when current densities over 20 mA cm⁻²) and larger peak power density (105 mW cm⁻²) than the referenced Pt/C + RuO₂ and most of advanced electrocatalysts (Table S3). To inspect the cycle stability (Fig. 4c), a charge/discharge current density of 5 mA cm⁻² was performed. The Fe-Co₄N@N-C electrocatalyst exhibits a negligible potential change after 220 cycles (> 36 h) and a very small voltage changes of 0.1 V even after 800 cycles

(Fig. S19), suggesting its excellent charge-discharge stability. This outstanding cycle stability may come from the good structure and surface chemical state stability of the electrocatalyst, which were also proved by XRD and XPS characterization (Fig. S20 and S21) after 100 cycles.

Based on the above results, we further construct rechargeable and flexible solid-state Zn-air batteries. The illustration of fabrication for the flexible solid-state Zn-air battery is shown in Fig. 5a. The self-supported Fe-Co₄N@N-C electrocatalyst, Zn foil and PAM-KOH-Zn (AC)₂ gel are used as air cathode, anode and electrolyte, respectively. This configuration can deliver considerable electronic conductivity and mechanical flexibility since it avoids the use of polymer binders and current collector. The open-circuit voltage is shown in Fig. S22. The Fe-Co₄N@N-C presents a higher open-circuit voltage of 1.34 V than the Pt/C + RuO₂ of 1.29 V. Fig. 5b displays two flexible solid-state Zn-air batteries connected in series to power a timer. The discharge polarization curve and the corresponding power density curve are shown in Fig. 5c and Fig. S23. Even if assembled as a flexible solid-state Zn-air battery, the Fe-Co₄N@N-C still demonstrates a maximum peak power density of 72 mW cm⁻³ superior than the referenced Pt/C + RuO₂ of 52 mW cm⁻³ and most of advanced electrocatalysts (as exhibited in Table S4). To further investigate the flexibility of the solid-state Zn-air battery, a charge-discharge cycle measurement under different bending angles at 4 mA cm⁻² is performed, as shown in Fig. 5d. When bended at 0°, 30° and 60°, the charge and discharge voltage present little degradation, which exhibits a better stability than the Pt/C + RuO₂ (Fig. S24) and many advanced flexible electrodes for solid-state Zn-air battery [45,46]. The electrochemical performance after several folds were shown in Fig. S25. The flexible Zn-air batteries exhibit similar discharge/charge profiles after 1 or 5 times of folding, indicating its reliable flexible stability. This results illuminate the potential application

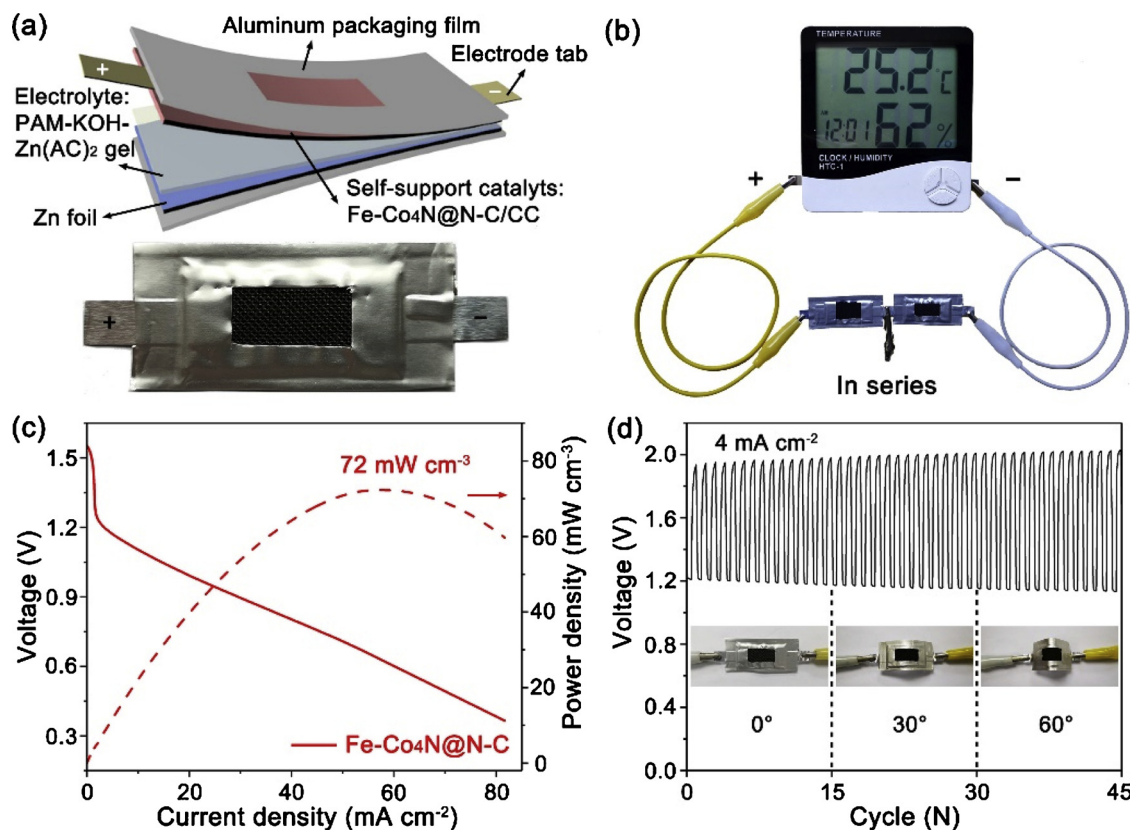


Fig. 5. a) The fabrication diagram of the flexible solid-state Zn-air battery, b) optical image of timer powdered by two flexible solid-state Zn-air batteries, c) discharge polarization curve and the corresponding power density curve, d) charge and discharge cycling curve of flexible solid-state Zn-air batteries under different bending conditions at 4 mA cm^{-2} .

prospect of self-supported Fe-Co₄N@N-C electrocatalyst as air cathode for solid-state Zn-air batteries in flexible devices.

4. Conclusions

In summary, we demonstrate the synthesis of the co-doped Fe-Co₄N@N-C nanosheets array derived from metal-organic framework precursor on carbon cloth as air cathode for reversible Zn-air battery. The ligand exchange reaction between 2-MIN and $[\text{Fe}(\text{CN})_6]^{3-}$ is crucial to promote the formation of Fe-doped Co₄N and specific N coordination modulated carbon. The surface chemical state analysis further proves that the Fe, N co-doping plays a vital role in enriching Pyridinic-N-M active sites, which can accelerate the charge transfer for improving ORR. The enriched Co³⁺ sites also motivate the formation of targeted *OOH intermediates during OER. As a result, the Fe-Co₄N@N-C electrocatalyst exhibits superior OER and ORR activity with extremely enhanced reaction kinetics. Moreover, the assembled liquid Zn-air battery exhibits a high specific energy density of 934 Wh kg⁻¹ with excellent cycling stability much superior to the referenced Pt and Ru-based Zn-air batteries. Flexible solid-state Zn-air battery also achieve a high volumetric power density of 72 mW cm^{-3} and good cycling durability under different bending states. This work provides a scalable and cost-efficient route to construct efficient dual-functional flexible electrode with enriched active sites for Zn-air batteries.

Conflict of interest

Nothing declared.

Acknowledgements

This work was supported by the National Natural Science

Foundation of China (21838003 and 51621002), the Social Development Program of Shanghai (17DZ1200900), the Shanghai Scientific and Technological Innovation Project (18JC1410600), the National Program for Support of Top-Notch Young Professionals, and the Fundamental Research Funds for the Central Universities (222201718002).

Appendix A. Supplementary data

Supplementary material related to this article can be found, in the online version, at doi:<https://doi.org/10.1016/j.apcatb.2019.117893>.

References

- [1] Z. Wang, D. Xu, J. Xu, X. Zhang, Chem. Soc. Rev. 43 (2014) 7746–7786.
- [2] P. Tan, B. Chen, H. Xu, H. Zhang, W. Cai, M. Ni, M. Liu, Z. Shao, Energy Environ. Sci. 10 (2017) 2056–2080.
- [3] Y. Li, J. Fu, C. Zhong, T. Wu, Z. Chen, W. Hu, K. Amine, J. Lu, Adv. Energy Mater. 9 (2019) 1802605.
- [4] W. Wan, X. Liu, H. Li, X. Peng, D. Xi, J. Luo, Appl. Catal. B: Environ. 240 (2019) 193–200.
- [5] X. Cai, L. Lai, J. Lin, Z. Shen, Mater. Horiz. 4 (2017) 945–976.
- [6] J. Yi, P. Liang, X. Liu, K. Wu, Y. Liu, Y. Wang, Y. Xia, J. Zhang, Energy Environ. Sci. 11 (2018) 3075–3095.
- [7] L. Tao, C. Lin, S. Dou, S. Feng, D. Chen, D. Liu, J. Huo, Z. Xia, S. Wang, Nano Energy 41 (2017) 417–425.
- [8] Q. Xu, Y. Liu, H. Jiang, Y. Hu, H. Liu, C. Li, Adv. Energy Mater. 9 (2019) 1802553.
- [9] X. Li, F. Dong, N. Xu, T. Zhang, K. Li, J. Qiao, ACS Appl. Mater. Inter. 10 (2018) 15591–15601.
- [10] P. Chen, K. Xu, Z. Fang, Y. Tong, J. Wu, X. Lu, X. Peng, H. Ding, C. Wu, Y. Xie, Angew. Chem. Int. Ed. 54 (2015) 14710–14714.
- [11] B. You, N. Jiang, M. Sheng, W.S. Drisdell, J. Yano, Y. Sun, ACS Catal. 5 (2015) 7068–7076.
- [12] H. Zhang, H. Jiang, Y. Hu, P. Saha, C. Li, Mater. Chem. Front. 2 (2018) 1462–1466.
- [13] C. Su, H. Cheng, W. Li, Z. Liu, N. Li, Z. Hou, F. Bai, H. Zhang, T. Ma, Adv. Energy Mater. 7 (2017) 1602420.
- [14] I. Amiuu, X. Liu, Z. Pu, W. Li, Q. Li, J. Zhang, H. Tang, H. Zhang, S. Mu, Adv. Funct.

Mater. 28 (2017) 1704638.

[15] H. Zhang, B. Chen, H. Jiang, X. Duan, Y. Zhu, C. Li, *Nanoscale* 10 (2018) 12991–12996.

[16] C. Guan, A. Sumboja, H. Wu, W. Ren, X. Liu, H. Zhang, Z. Liu, C. Cheng, S.J. Pennycook, J. Wang, *Adv. Mater.* 29 (2017) 1704117.

[17] C. Guan, A. Sumboja, W. Zang, Y. Qian, H. Zhang, X. Liu, Z. Liu, D. Zhao, S.J. Pennycook, J. Wang, *Energy Storage Mater.* 16 (2019) 243–250.

[18] Q. Xu, H. Jiang, H. Zhang, Y. Hu, C. Li, *Appl. Catal. B: Environ.* 242 (2019) 60–66.

[19] Y. Liang, H. Wang, P. Diao, W. Chang, G. Hong, Y. Li, M. Gong, L. Xie, J. Zhou, J. Wang, T.Z. Regier, F. Wei, H. Dai, *J. Am. Chem. Soc.* 134 (2012) 15849–15857.

[20] X. Wang, J. Liu, Z. Liu, W. Wang, J. Luo, X. Han, X. Du, S. Qiao, Jing Yang, *Adv. Mater.* 30 (2018) 1800005.

[21] F. Meng, H. Zhong, D. Bao, J. Yan, X. Zhang, *J. Am. Chem. Soc.* 138 (2016) 10226–10231.

[22] Y. Hou, Z. Wen, S. Cui, S. Ci, S. Mao, J. Chen, *Adv. Funct. Mater.* 25 (2015) 872–882.

[23] Q. Wang, Y. Ji, Y. Lei, Y. Wang, Y. Wang, Y. Li, S. Wang, *ACS Energy Lett.* 3 (2018) 1183–1191.

[24] C. Li, M. Wu, R. Liu, *Appl. Catal. B: Environ.* 244 (2019) 150–158.

[25] K. Kordek, L. Jiang, K. Fan, Z. Zhu, L. Xu, M. Al-Mamun, Y. Dou, S. Chen, P. Liu, H. Yin, P. Rutkowski, H. Zhao, *Adv. Energy Mater.* 9 (2019) 1802936.

[26] H. Wang, C. Tang, B. Wang, B. Li, X. Cui, Q. Zhang, *Energy Storage Mater.* 15 (2018) 124–130.

[27] E. Hu, J. Ning, D. Zhao, C. Xu, Y. Lin, Y. Zhong, Z. Zhang, Y. Wang, Y. Hu, *Small* 14 (2018) 1704233.

[28] X. Zhu, T. Jin, C. Tian, C. Lu, X. Liu, M. Zeng, X. Zhuang, S. Yang, L. He, H. Liu, S. Dai, *Adv. Mater.* 29 (2017) 1704091.

[29] L. Chen, H. Jiang, H. Jiang, S. Guo, Y. Hu, C. Li, *Adv. Energy Mater.* 7 (2017) 1602782.

[30] Q. Wang, Y. Lei, Z. Chen, N. Wu, Y. Wang, B. Wang, Y. Wang, *J. Mater. Chem. A* 6 (2018) 516–526.

[31] K. Yoon, K. Shin, J. Park, S. Cho, C. Kim, J. Jung, J. Cheong, H. Byon, H. Lee, I. Kim, *ACS Nano* 12 (2018) 128–139.

[32] L. Wang, W. Zhang, X. Zheng, Y. Chen, W. Wu, J. Qiu, X. Zhao, X. Zhao, Y. Dai, J. Zeng, *Nat. Energy* 2 (2017) 869–876.

[33] Q. Xu, H. Jiang, H. Zhang, H. Jiang, C. Li, *Electrochim. Acta* 259 (2018) 962–967.

[34] X. Liu, L. Xu, G. Xu, W. Jia, Y. Ma, Y. Zhang, *ACS Catal.* 6 (2016) 7611–7620.

[35] I. Amiinu, X. Liu, Z. Pu, W. Li, Q. Li, J. Zhang, H. Tang, H. Zhang, S. Mu, *Adv. Funct. Mater.* 28 (2018) 1704638.

[36] H. Zhong, K. Li, Q. Zhang, J. Wang, F. Meng, Z. Wu, J. Yan, X. Zhang, *NPG Asia Mater.* 8 (2016) e308.

[37] Z. Chen, Y. Li, L. Lei, S. Bao, M. Wang, H. Liu, Z. Zhao, M. Xu, *Catal. Sci. Technol.* 7 (2017) 5670–5676.

[38] S.G. Peera, A. Arunchander, A.K. Sahu, *Nanoscale* 8 (2016) 14650–14664.

[39] L. Yang, L. Shi, D. Wang, Y. Lv, D. Cao, *Nano Energy* 50 (2018) 691–698.

[40] F. Meng, Z. Wang, H. Zhong, J. Wang, J. Yan, X. Zhang, *Adv. Mater.* 28 (2016) 7948–7955.

[41] J. Zhao, N. Fu, R. Liu, *ACS Appl. Mater. Interfaces* 10 (2018) 28509–28516.

[42] X. Gao, J. Yang, K. Song, W. Luo, S. Dou, Y. Kang, *J. Mater. Chem. A* 6 (2018) 23445–23456.

[43] S. Han, X. Hu, J. Wang, X. Fang, Y. Zhu, *Adv. Energy Mater.* 8 (2018) 1800955.

[44] H. Zhang, H. Jiang, Q. Xu, Y. Hu, C. Li, *Chem. Eng. Sci.* 195 (2019) 665–670.

[45] B. Li, S. Zhang, B. Wang, Z. Xia, C. Tang, Q. Zhang, *Energy Environ. Sci.* 11 (2018) 1723–1729.

[46] S. Zeng, X. Tong, S. Zhou, B. Lv, J. Qiao, Y. Song, M. Chen, J. Di, Q. Li, *Small* 14 (2018) 1803409.